Microstructural Evaluation of Low and High Duty Cycle Nd:YAG Laser Beam Welds in 2024-T3 Aluminum

Changes in weld microstructure due to an increased duty cycle produced acceptable laser weld morphology in a hot-tear-sensitive alloy

BY J. O. MILEWSKI, G. K. LEWIS AND J. E. WITTIG

ABSTRACT. The propensity for hot tearing and porosity in pulsed Nd-YAG laser beam welding of 2024-T3 aluminum was observed to vary with "beam on" duty cycle. High average laser output power of 1 kW and variation in duty cycle were achieved by multiplexing a system of three 400-W average power Nd:YAG lasers with fiber-optic delivery. Operating this system with a greater than 60% duty cycle eliminated the severe hot tearing and gross porosity that occurred in lower duty cycle welds made under otherwise identical conditions. Microstructural characterization of the low and high duty cycle welds identified differences in weld morphology directly related to hot-crack susceptibility. Solute segregation and the distribution of low melting point phases are dependent upon the solidification history. In addition, manipulating the input power alters the solidification-related stress state developed in the weld fusion zone. Appropriate adjustment of the process parameters, e.g., duty cycle, optimizes the solidification velocity, thermal gradients, and stress state in the weld fusion zone in order to prevent hot tearing in this crack-susceptible aluminum alloy.

Introduction

Recent developments (Ref. 1) in Nd:YAG laser beam welding systems have enabled this process to produce welds at average powers above 1 kW. The increased available power at 1.06 μm allows deeper penetration in materials of higher thermal diffusivity and reflectivity such as aluminum and copper. While these welding power ranges have been achieved by CO_2 welding systems for a number of years, CO_2 systems suffer from limited laser power coupling efficiency, complex optical trains, and high equipment costs (Ref. 2). Flexible fiber-optic delivery systems have enhanced the attractiveness of Nd:YAG systems. Multiplexing of pulsed lasers through optical fibers provides control of power inputs over a wide range of weld pulse shapes, frequencies and duty cycles where the duty cycle is defined as the percentage of "beam on" time over one period of pulsing frequency.

Pulsed power welding was developed in conventional arc processes to limit heat input and reduce the effects of distortion. However, under certain conditions, pulsed arc welding has been found to intensify hot-tearing problems (Ref. 3). Similar results have been observed in pulsed laser beam welding. While pulsed laser beam welding is proposed to reduce heat input and control grain orientation (Ref. 4), the tendency for hot tearing has in some cases been observed to increase (Ref. 5) in hot-crack-sensitive aluminum alloys. Cieslak (Ref. 5) has proposed that thermally induced stress gradients in pulsed Nd:YAG laser beam welds were primarily responsible for hot tearing and not microstructural changes such as the observed loss of magnesium from the fusion zone.

Hot tearing theory as it relates to the weldability of aluminum alloys has been reviewed and extended by Cross (Ref. 6) and others (Refs. 7, 8). In general, these treatments are limited to high-purity binary or ternary alloy systems so as to avoid the complexities present in commercial alloys. Comparison between various commercial alloys and heat treatments has been achieved by the application of empirical tests that utilize induced strain upon solidification in order to rank their hot-crack sensitivity (Refs. 9, 10). It is clear from these tests that differences in the concentration of alloying elements and impurities affect hot-crack susceptibility (Refs. 6, 8, 11). Adjusting the alloy composition changes the volume fraction and distribution of lower melting point secondary phases believed to play a role in the hot cracking phenomenon. However, microstructural development of the weldment is also strongly dependent on the welding process parameters. Variations in the weldability of a specific material can be obtained by changing the process parameters that affect the resultant solidification microstructure.

KEY WORDS

Microstructure
Nd:YAG Laser Welds
Low/High Duty Cycle
2024-T3 Aluminum
Hot Tearing
Porosity
Weld Morphology
Hot Crack Susceptibilty
Solidification His.
Thermal Gradients

J. O. Milewski and G. K. Lewis are with Los Alamos National Laboratory, Los Alamos, N.Mex., and J. E. Wittig is with Vanderbilt University, Nashville, Tenn.

Table 1 — Alloy 2024 Composition

	% min	% max
Cu	3.8	4.9
Mg	1.2	1.8
Mn	0.30	0.9
Fe	—	0.50
Si	—	0.50
Zn	—	0.25
Ti	—	0.15
Cr	—	0.10
Other	—	0.05
total	—	0.15
Al	Remainder	

weight percent

Higher average power Nd:YAG laser beam welding systems now provide the ability to extend the range of their processing parameters to include high-duty-cycle welding. It is therefore useful to characterize differences in the weld morphology as a result of variations in duty cycle. Aluminum Alloy 2024 in the T3 condition is an ideal commercial material for this study due to its high susceptibility to hot tearing and the availability of complementary welding studies performed using this material (Ref. 12). The topic of the current investigation is a microstructural comparison between Nd:YAG laser beam welds made in 2024-T3 aluminum with low and high duty cycles.

Experimental Procedure

Table 1 lists the established Aluminum Association compositional range of the 2024-T3 alloy. Sheared plate test specimens 3 mm (0.12 in.) thick and 100 X 100 mm (3.9 X 3.9 in.) were cleaned and degreased by dipping in solutions of NaOH and HNO_3. Autogenous bead-on-plate welds were made parallel to the rolling direction with a Lumonics 3-into-1 laser system consisting of three 400-W pulsed Nd:YAG lasers. A fiber-optic delivery system and welding head combine the three laser beams into a single 1.0-mm (0.039-in.) spot at the focal point of a 50-mm (1.95-in.) focal length lens. Single axis translation of the part was provided by an Anorad multi-axis translation table and controller. Travel speed was constant at 3.15 mm/s (7.4 in./min). Argon gas was used to shield the molten weld pool by an oblique mounted gas diffuser.

The individual lasers can be synchronized to fire sequentially or simultaneously. A full range of pulse shapes, widths and powers can be computer controlled within the power capabilities of the equipment. Preliminary weld tests were performed to evaluate the effect of various combinations of laser pulse powers, pulse duration, pulse sequencing (sequential vs. simultaneous), and pulse repetition rate. Combination of the direct weld input parameters of pulse duration and pulse repetition rate were used to calculate the duty cycle as percent of beam-on time for a repetition cycle. Table 2 shows the weld schedules for 20 weld tests.

These welds were aged at room temperature for more than two weeks prior to metallographic preparation. Two weld schedules, representative of low and high duty cycle conditions, were chosen for detailed microstructural evaluation. Diagrams depicting the pulse shape, duty cycle and power of these weld schedules are shown in Fig. 1. The low-duty-cycle (LDC) welding conditions consisted of an average power per cycle of 1020 W where all three lasers fired 340 W simultaneously for 6.6 ms at a repetition rate of 50 Hz. This resulted in a duty cycle of 33%. The high- duty-cycle (HDC) weld fired the 340 W pulses sequentially to produce a duty cycle of 99% with equivalent energy input per second. To test for reproducibility, three separate sets of welds were produced using these two schedules.

Microstructural characterization of the LDC and HDC weldments was performed by using optical microscopy, scanning electron microscopy (SEM) and transmission electron microscopy (TEM). Samples, prepared from the three orthogonal orientations of the weld bead, were polished and etched in Kellers reagent for optical microscopy and SEM observation. In addition, tensile samples taken transverse to the weld direction were fractured and examined in the SEM. Specimens for TEM analysis were prepared by first slicing sections parallel to the plate surface and then grinding on silicon-carbide paper to known distances from the surface. Disk samples, 2.3 or 3 mm in diameter, were punched from the sliced material, reduced in thickness by mechanical grinding, and thinned to electron transparency by twin-jet electropolishing in 25% HNO_3 and 75% methanol solution at –40°C and 15 V. These samples were analyzed with a Philips CM20T operating at 200 kV. The CM20 was equipped with an x-ray energy dispersive spectrometer (EDS) for semiquantitative

Table 2 — Weld Test Data for 3 into 1 ND: YAG Laser System Aluminum Alloy 2024 T-3 Bead-on-Plate Melt Welds

	Firing Mode[a]	Laser 1 watts, msec	Laser 2 watts, msec	Laser 3 watts, msec	Average Power, watts	Repetition Rate Hz	Duty Cycle %	Cracking Observed
1	sim	400, 10	400, 10	400, 10	1200	20	20	N.G.
2	sim	400, 10	400, 10	400, 10	1200	20	20	yes
3	seq	400, 10	400, 10	400, 10	1200	20	60	no
4	sim	400, 5	400, 5	400, 5	1200	50	25	yes
5	sim	400, 5	400, 5	400, 5	1200	50	25	yes
6	sim	350, 5	350, 5	350, 5	1050	50	25	yes
7	seq	350, 5	350, 5	350, 5	1050	50	75	no
8	seq	350, 5	350, 5	0, 0	700	50	50	yes
9	sim	350, 5	0, 0	0, 0	350	50	25	yes
10	sim	340, 7	340, 7	340, 7	1020	50	35	yes
11	seq	340, 7	340, 7	340, 7	1020	50	100	no
12	seq	340, 7	340, 7	0, 0	700	50	70	no
13	seq	190, 7	340, 7	190, 7	720	50	100	no
14	seq	190, 7	387, 7	190, 7	767	50	100	no
15	seq	190, 7	300, 7	190, 7	680	15	31	yes
16	seq	150, 7	300, 7	150, 7	600	15	31	yes
17	seq	225, 7	300, 7	225, 7	750	15	31	yes
18	seq	300, 7	300, 7	300, 7	900	15	31	yes
19	seq	400, 7	400, 7	400, 7	1200	15	31	yes
20	seq	210, 7	400, 7	210, 7	820	15	31	yes

travel speed 3.15 mm/sec
argon gas shield, 50-mm focusing lens
(a) simultaneous, sequential

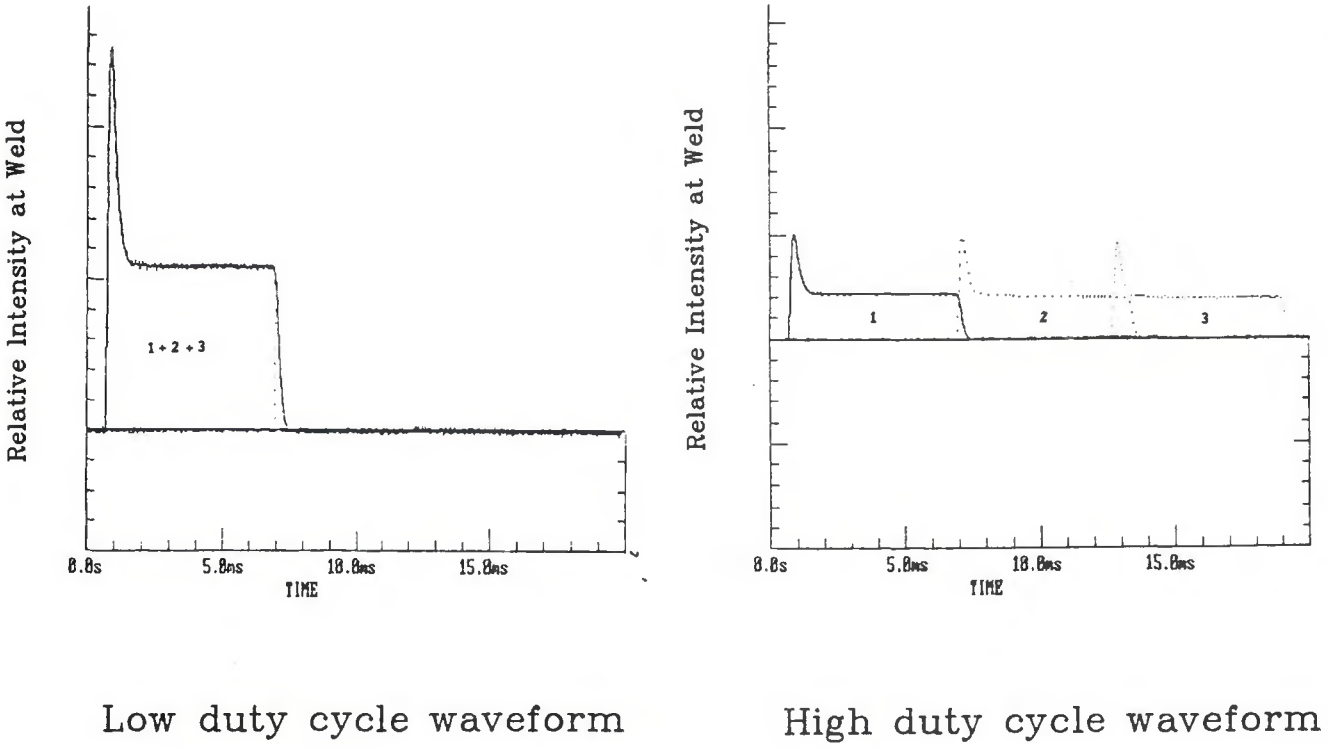

Fig. 1 — Representative laser intensity profiles.

chemical analysis and a scanning attachment (STEM) with both secondary electron and transmitted electron detectors.

Results

Table 2 summarizes the occurrence of hot tearing for the various duty cycles employed in this investigation. Macroscopic inspection of the weld beads for the 20 weld schedules revealed large centerline cracks as well as secondary cracks for duty cycles less than 60%. From these various duty cycles, the two weld schedules described in Fig. 1 represent extremes of the duty cycle conditions. The low duty cycle (LDC) of 33%, which fired all three lasers simultaneously, resulted in a severely cracked weld bead. For the high duty cycle (HDC) of 99%, where the lasers were fired sequentially, there was no visual evidence of hot tearing on the weld bead surface.

The optical micrographs in Fig. 2A and B show transverse cross-sections of the fusion zones (FZ) for the LDC and HDC welds. The LDC weld exhibited a crack extending along the weld centerline from the weld bead to near the weld root. The HDC weld again displayed no evidence of cracking. Longitudinal sections showed that the porosity in the LDC weld was randomly spaced and typically 10 to 500 microns in size. Similar samples from the HDC weldment exhibited virtually no porosity greater than 50 microns in size. Further inspection of the LDC weld showed that the hot cracks would often deviate from the centerline to intersect with the large pores. These observations were reproduced on three different sets of welds made under identical conditions. The solidification banding seen in both welds corresponds to the pulsing period of 20 ms. Successive meltback of previ-

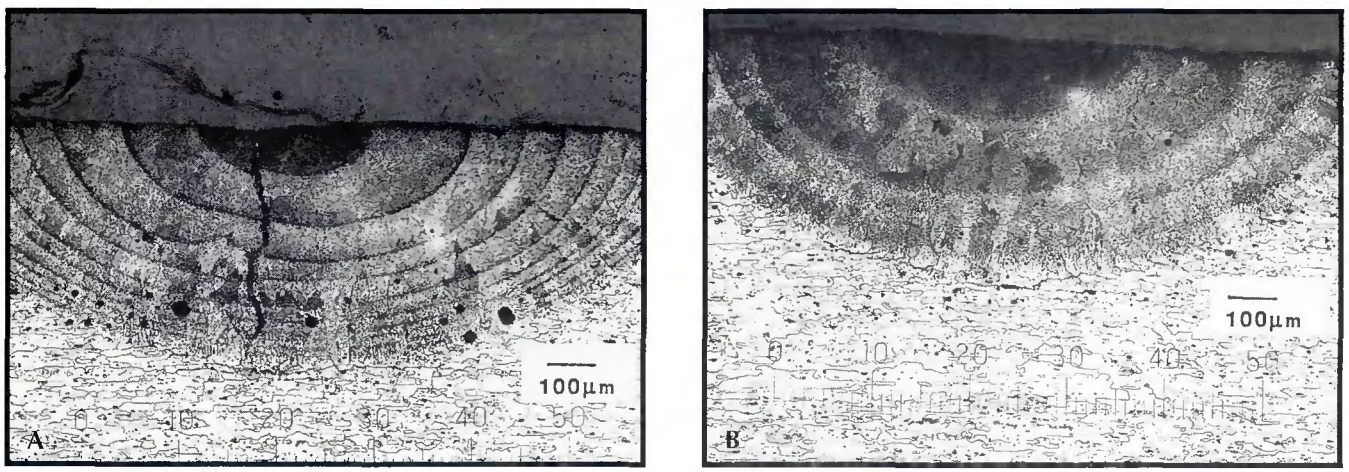

Fig. 2 — A — Transverse cross-section of low- duty-cycle weld; B — transverse cross-section of high-duty-cycle weld.

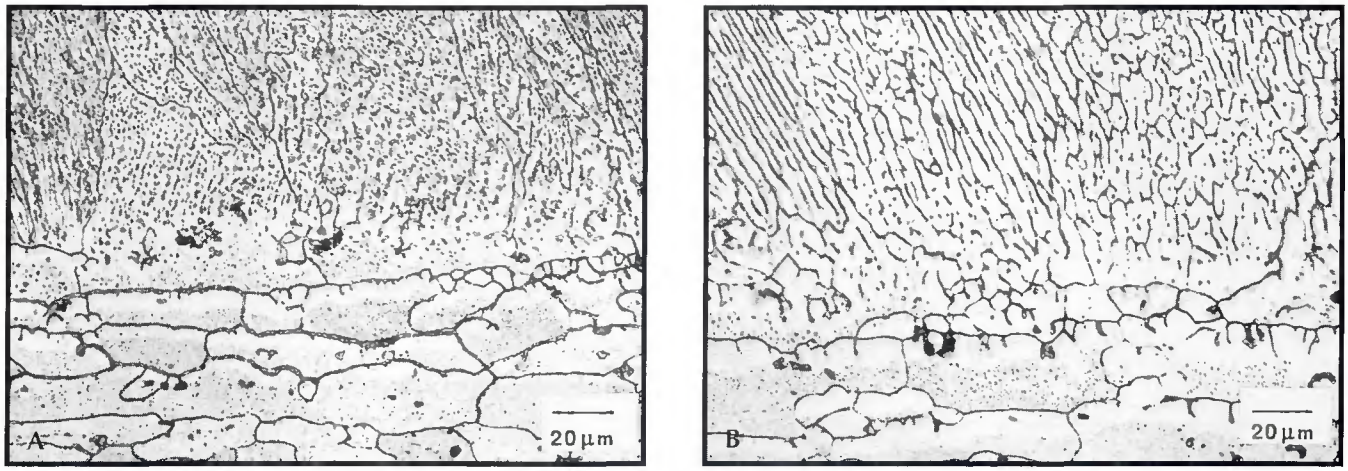

Fig. 3 — A — Longitudinal section of LDC weld showing a refined structure; B — longitudinal section of HDC weld showing a coarse structure.

ously solidified fusion interface and changes in the microstructure due to the interruption in the solidification rate produces these bands in the solidification structure.

Longitudinal cross-section optical micrographs in Fig. 3A and B show a higher magnification view of the solidification structure. Dissimilar distribution of the interdendritic material (dark contrast phase) in the FZ of the HDC weld compared to the LDC weld clearly shows the variation in solidification history from these two welding schedules. The finer distribution of interdendritic material in the FZ of the LDC weld is indicative of a higher cooling rate compared to the HDC condition. In fact, it may be more accurate to describe the LDC FZ as a cellular structure with an intercellular phase. In addition, the HDC weld has a more pronounced heat-affected zone (HAZ) than the LDC weld.

Examination of the fracture surfaces from the tensile specimen also revealed important details concerning the solidification history and cooling rates. Fig. 4 shows a scanning electron micrograph of a fracture surface from the LDC weld where the interior of a hot tear that occurred during welding has been exposed. The smooth surface represents the dendritic solidification structure where the interdendritic liquid has coated the hot-cracked surface. Measurement of the secondary dendrite arm spacing on this fracture surface permits an estimation of the cooling rate. Referring to the data of Munitz for Al-4.5 wt-% Cu alloys (Ref. 13), an average secondary dendrite arm spacing of approximately one micron corresponds to a cooling rate of about 10^5 K/s. This value agrees with the finite difference heat flow modeling done by Korzekwa that calculated a 2.5 X 10^5 K/s cooling rate after a 1-kW laser pulse in an aluminum alloy (Refs. 14, 15).

Fig. 4 — SEM fractograph of LDC weld showing exposed dendritic surface.

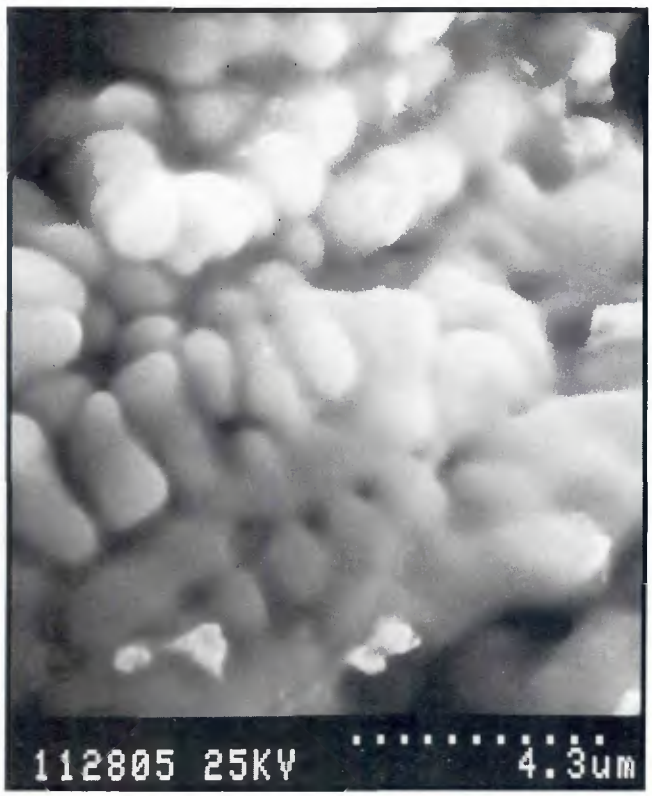

The remainder of the LDC weld fracture surface exhibited a brittle fracture mode. Figure 5A shows that the fracture path in the FZ followed an interdendritic route. In Fig. 5B, the fracture intersected one of the large pores present in the FZ. In contrast, the HDC weld fractured with a ductile mode through the HAZ adjacent to the FZ. Figure 6 shows the fracture surface of a tensile sample from the HDC weldment. Fracture in the HAZ is typical for welds in Al-Cu alloys due to loss of the strengthening precipitates through dissolution.

Figure 7 is a secondary electron image of the surface of a TEM sample from the HDC weldment. This thin foil region is a section parallel with the plate surface taken from about 175 microns below the weld surface. Figure 8A–C shows representative bright field (BF) TEM images of the base material, HAZ, and FZ from the HDC weld. The base microstructure consists of a fine dispersion of semi-coherent Al_2Cu theta precipitates in an aluminum matrix having a high dislocation density. These precipitates are absent in the HAZ where the second phase has occurred due to the welding process. The FZ in the HDC weld is characterized by high-angle grain boundaries covered with precipitates and an interdendritic network of second-phase particles. Figure 9A and B shows the contrast in the distribution of the second phase in the FZ of the HDC

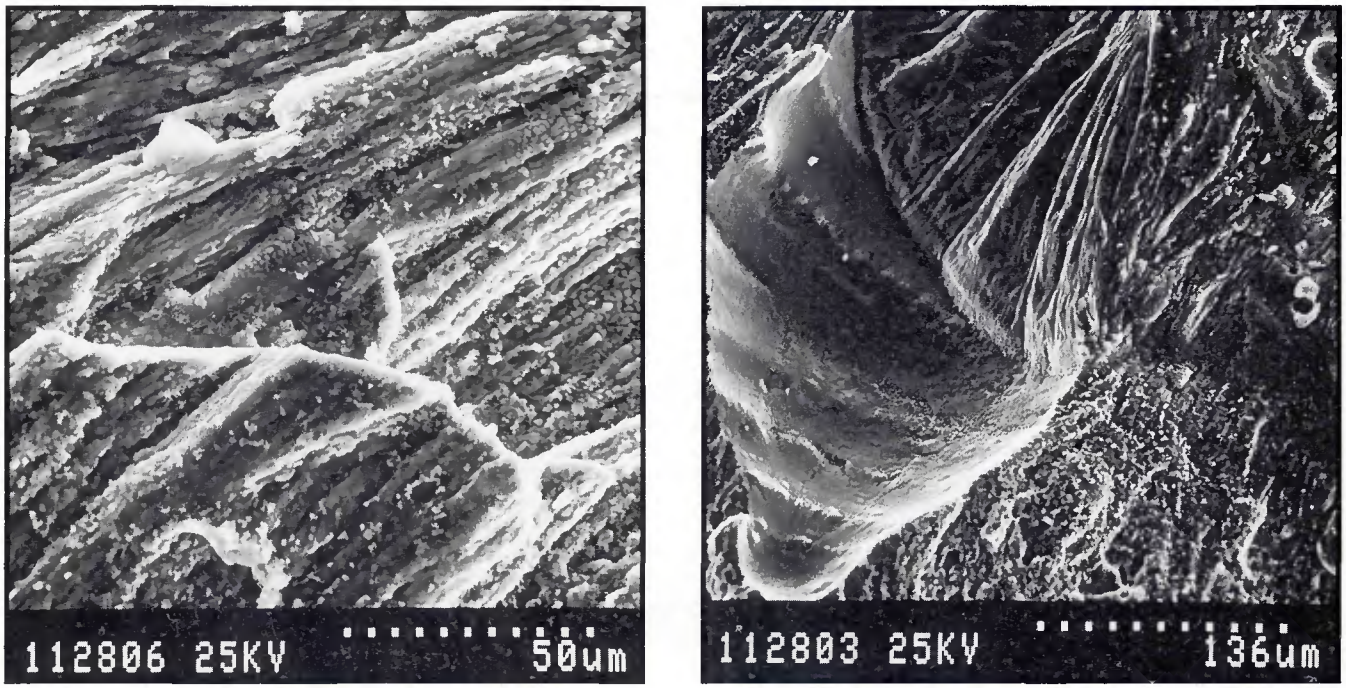

Fig. 5 — SEM fractograph of LDC weld showing: Left — Solidification patterns; right — pore growth over successive laser pulses.

and LDC welds. Compared to the interdendritic network in the FZ of the HDC weld, the interdendritic/cellular phase in the LDC weld is isolated at low-angle cell boundaries.

A semiquantitative STEM-EDS composition analysis of the grain boundary and matrix precipitates identified a variety of precipitate types. Although the majority were Al-Cu based, Al-Si-rich precipitates (probably oxides) were also detected. At least two types of Al-Cu precipitates were present. The theta phase based on the Al_2Cu body-centered tetragonal structure contained additions of Mg and Fe with a typical composition in atomic percent of Al, 25% Cu, 9% Mg, 1% Fe. A second phase, believed to be a highly microtwinned hexagonal phase, contained larger amounts of Fe and Mn with an average composition of Al, 20% Cu, 7% Fe, 2% Mn (Ref. 15). A comparison between the HDC and LDC average FZ grain boundary precipitate composition showed that the precipitates in the HDC weld were enriched with larger amounts of Fe, Mn and Mg than the corresponding LDC precipitates.

Discussion

The cooling rate of the weld fusion zone is dependent upon the thermal gradients in the liquid and solid and the velocity of the solid/liquid interface. Compared to the HDC welding conditions where synchronization of the three lasers operated with a virtually continuous 340-W power output, the LDC welding conditions produced a significantly larger thermal gradient in the material by pulsing over 1 kW of power in a 6.6 ms time interval. The subsequent higher cooling rate developed in the LDC weld (estimated to be on the order of 10^5 K/s) accounts for the refinement in the distribution of the interdendritic second phase as well as the smaller amount of solute elements present within the precipitation compared to the HDC weldment. Rejection of solute atoms ahead of the solid/liquid solidification front requires adequate time for diffusion. The faster the solidification rate, the greater is the probability that solute atoms will be trapped within the growing solid.

During solidification, stresses are developed in the fusion zone of the weld from thermal contraction and solidification-induced shrinkage. Hot tearing occurs when the partially solidified material can no longer withstand these

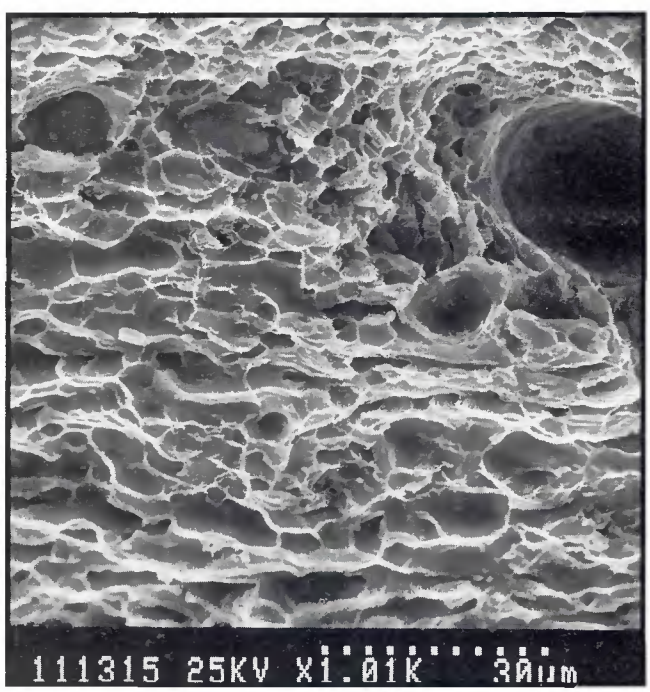

Fig. 6 — Fracture surface within HAZ of HDC weld.

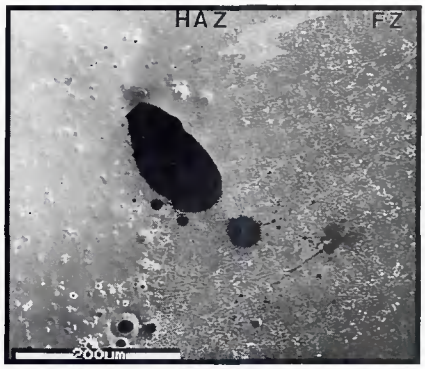

Fig. 7 — Secondary electron image of TEM sample taken from HDC weld showing (from left to right): base material, HAZ and FZ.

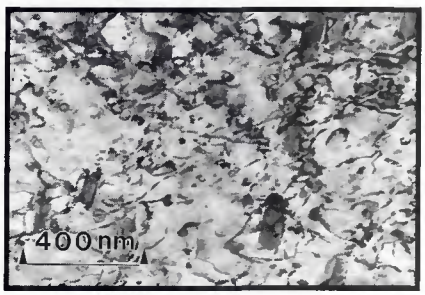

A

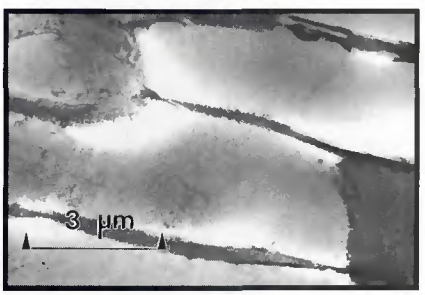

B

C

Fig. 8 — Bright field (BF) TEM images from HDC weld. A — Base material; B — heat-affected zone; C — fusion zone.

stresses. As long as sufficient volumes of a low-melting-point phase are present to fill the growing hot tear, the final weldment will be sound. This is the case that was observed for the HDC weld. The smaller thermal gradient and lower cooling rate in the HDC weld produced both a reduced stress state as well as a greater opportunity for the backfilling of the developing cracks. Direct evidence of this could be observed by the larger coverage of precipitation on the high-angle grain boundaries of the HDC weld compared to the LDC weld.

A final consideration is the effect of porosity on the susceptibility for hot tearing in this alloy. The higher temperatures developed during the pulsed LDC mode could account for the larger amount of porosity observed in these welds compared to the fusion zone of the HDC weld. Expanding gases trapped within the solidifying material would increase the already critical stress state responsible for the hot tearing. Clearly, by careful control of the processing parameters, it is possible to successfully weld a hot-tear-sensitive alloy such as 2024-T3 with Nd:YAG laser beam welding technology. Further work is required to understand the interrelated variables such as solidification rate, stress state, and porosity formation in order to optimize this welding process.

Conclusion

Through the use of Nd:YAG laser beam welding equipment, which allows beam on duty cycle changes up to 100% and average powers up to 1 kW, appropriate adjustment of duty cycle has been shown to affect the weld microstructure significantly enough to produce sound welds in 2024-T3 aluminum, which is susceptible to hot tearing and porosity at lower duty cycles. Microstructural characterization of low- and high-duty-cycle laser beam welds identified differences in weld morphology and defect formation that fit within the framework of existing solidification theory.

Acknowledgment

This work was performed under the U.S. Department of Energy contract W-7405-ENG-36.

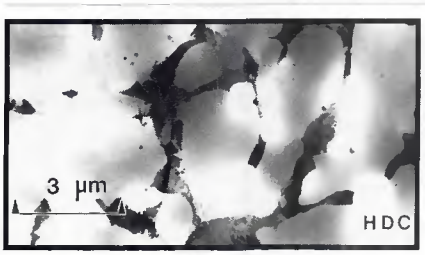

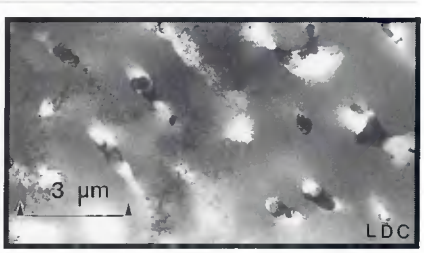

Fig. 9 — Second phase distribution in: Left — HDC weld fusion zone; right — LDC weld fusion zone.

References

1. McFadden, G., and Filgas, D. M. Designing ND:YAG lasers for higher power. *Lasers and Optronics*. August 1990: 33–40.

2. Kaukler, W. F., Workman, G. L., and Plaster, T. Laser welding in space. *Recent Trends in Welding Science and Technology*. Edited by S. A. David and J. M. Vitek. ASM, Materials Park, Ohio. 1990: 463-467.

3. Patterson, R. A., and Milewski, J. O. GTA weld cracking — Alloy 625 to 304L. *Welding Journal*. 64(8): 227s to 231s.

4. Albright, C. E. Pulsed CO_2 laser welding. *Trends in Welding Research*. Edited by S. A. David. ASM, Materials Park, Ohio. 1982: 653–665.

5. Cieslak, M. J., and Fuerschbach, P. W. On the weldability, composition, and hardness of pulsed and continuous Nd-YAG laser welds in aluminum Alloys 6061,5456, and 5086. *Metallurgical Transactions B*, 1988, 19B: 319.

6. Cross, C. E. Weldability of aluminum-lithium alloys: an investigation of hot tearing mechanisms. Ph. D. thesis, Metallurgical Engineering. Colorado School of Mines, Golden, Colorado. August 1986.

7. Clyne, T. W., and Davies, G. J. Comparison between experimental data and theoretical predictions relating to dependence of solidification cracking on composition. *TMS Proc. Int. Conf. Solidification — Sheffield*. 1979: 275–279

8. Arata, Y., Matsuda, K., Nakata, K., and Sasaki, I. Solidification crack susceptibility of aluminum alloy weld metals — Report I. *Trans. JWRI*. 1976, 5: 53–67.

9. Goodwin, G. M. A new hot cracking test: the Sigamajig. *Welding Journal*. 66(2): 335.

10. Lundin, C. D., Lingenfelter, A. C., Grotke, G. E., Lessman, G. G., and Matthews, S. J. The Varestraint test. *WRC Bulletin 280*, Welding Research Council. New York, New York. August 1982.

11. Aluminum: properties and physical metallurgy. Edited by J. E. Hatch. ASM, Materials Park, Ohio. 1984.

12. Katayama, S., et al. Laser weldability of aluminum alloys. Recent Trends In Welding Science and Technology. Edited by S. A. David, J. M. Vitek. ASM, Materials Park, Ohio. 1990: 687–691.

13. Munitz, A. Microstructure of rapidly solidified laser molten Al-4.5 wt pct Cu surfaces. Metallurgical Transactions B. 1985,16B: 149–161.

14. Cremers, D. A., Lewis, G. K., Korzekwa, D. R. Measurement of energy deposition during pulsed laser welding. *Welding Journal* 70(7): 159-s to 167-s.

15. Lewis, G. K. Los Alamos National Laboratory. Private communication, unpublished data. January 1991.

16. Kim, D. H., Chattopadhyay, K., and Cantor, B. Quasicrystalline and related crystalline phases in a rapidly solidified 2024-2Li aluminum alloy. *Acta Metall. Mater.* 1991, 39(5): 859–875.